PNAS

www.pnas.org

Supplementary Information for

Spatial patterns of climate change across the Paleocene-Eocene Thermal Maximum

Jessica E. Tierney, Jiang Zhu, Mingsong Li, Andy Ridgwell, Gregory J. Hakim, Christopher J. Poulsen, Ross D. M. Whiteford, James W. B. Rae, and Lee R. Kump

Jessica E. Tierney.
E-mail: jesst@arizona.edu

This PDF file includes:

Supplementary text
Figs. S1 to S10 (not allowed for Brief Reports)
Tables S1 to S2 (not allowed for Brief Reports)
Legends for Dataset S1 to S2
SI References

Other supplementary materials for this manuscript include the following:

Datasets S1 to S2

Supporting Information Text

Supporting Materials & Methods

Proxy data compilation. The data used in this reconstruction derive primarily from the deepMIP compilation of pre-PETM and PETM proxy indicators for temperature (1). These data include the δ^{18}O of well-preserved ("glassy") planktic foraminifera, the Mg/Ca of foraminifera, TEX$_{86}$, and the terrestrial MBT5$'_{Me}$ proxy. We targeted these particular proxies because we have previously developed Bayesian forward models for each of them, which facilitates the use in the data assimilation framework (2–5). Generally speaking, we followed deepMIP guidance for assessing which proxy values fell within the pre-PETM and PETM time periods; any adjustments to this assumption are documented in the "assessment" column of the proxy data file (Dataset S1). We also incorporated additional, more recently published studies (6–12), referring to the original publications when assigning data to each target time interval. δ^{18}O and Mg/Ca analyses conducted on single foraminifera were pre-averaged within their respective core depths before calculating prePETM and PETM averages. The Otaio Gorge MBT5$'_{Me}$ data from the lignite and marine sediment beds, respectively, were treated as separate estimates given that there is a lithological offset (12).

In the deepMIP compilation, TEX$_{86}$ data with BIT index > 0.4 (an indicator of terrestrial GDGT input, c.f. (13)) and methane index (MI) > 0.5 (an indicator of GDGT input from methanotrophs, c.f. (14)) were excluded from the prePETM and PETM averages. Δ Ring Index (RI) values were assessed and flagged if greater than 0.3, but data were not necessarily excluded on the basis of ΔRI alone. We follow this guidance with a few exceptions, noting that none of these quality indices have agreed-upon universal cut-off values and the decision of what to include/exclude can be site-specific. From the Harrell Core dataset, we opted to include three late Paleocene datapoints with a MI < 0.5 (in spite of BIT values of ca. 0.8) in the interest of having the prePETM represented at that site (otherwise, all prePETM data would be excluded). The average TEX$_{86}$ value of these three datapoints is 0.738, which is similar to the prePETM values at other eastern North American sites (Bass River and Wilson Lake; 0.748 and 0.700, respectively), suggesting that the data are reasonable. From the ACEX dataset, we used the updated dataset of ref. (8) and the same PETM averaging interval as deepMIP, but, again in the interest of having the prePETM represented at this site, included two late Paleocene datapoints that had BIT < 0.4, MI < 0.5, and ΔRI < 0.35. At the Fur site, given that the recent study of ref. (6) measured TEX$_{86}$ on the same section as the older study of ref. (15), largely replicating the original result but at higher resolution, the data from ref. (15) are excluded so as to avoid duplication. From ref. (6), we included all of the late Paleocene data (which have BIT values from 0.27–0.51 but normal MI and ΔRI values) except for four data points from the prePETM average that had more elevated BIT (0.54–0.81) and ΔRI > 0.35 (labeled in red dots in Figure 5 of ref. (6)). At the Chicxulub crater drill site (M0077A) there is only one data point from the prePETM available. We included it, because in spite of a ΔRI of 0.7 it has low BIT (0.16) and MI (0.18).

For the δ^{18}O and Mg/Ca of foraminifera, we collected data measured on species thought have lived in the mixed layer, close to the ocean surface, namely *Morozovella spp.* and *Acarinina spp.*. However, we subsequently discovered that inclusion of *Acarinina spp.* in the data assimilation systematically reduced the change in global mean surface temperature (GMST) during the PETM (see further discussion below). Several previous studies have suggested that *Acarinina spp.* migrated to deeper waters during the PETM event, as its δ^{18}O composition appears similar to that of the thermocline-dwelling *Subbotina spp.* (16–18). Our data compilation indicates that the δ^{18}O of *Acarinina spp.* during the PETM is, on average, 0.36‰ higher (i.e., cooler) than *Morozovella spp.* at the same sites, and likewise, that Mg/Ca values for *Acarinina spp.* are 0.31 mmol/mol lower. We therefore decided to exclude *Acarinina spp.* from our final reconstruction.

The assimilation uses the average proxy value for each timeslice. The standard deviation of this value and number of datapoints contributing are documented in the proxy data file (Dataset S1).

Climate model simulations. The prior climate simulations used the fully-coupled, isotope-enabled Community Earth System Model version 1.2 (iCESM 1.2) (19). iCESM simulates the transport and transformation of stable water isotopes (δ^{18}O and δD) in all component models (20). All the iCESM simulations have a horizontal resolution of 1.9° × 2.5° (latitude × longitude) in the atmosphere and land, and a nominal 1° displaced-pole Greenland grid for the ocean. The simulations with 3X, 6X, and 9X preindustrial CO_2 employed boundary conditions from deepMIP (21), which include reconstructions of Eocene paleogeography, land-sea mask, and vegetation distribution (22), and preindustrial non-CO_2 greenhouse gas concentrations, solar constant, orbital parameters, soil properties, and natural aerosol emissions. Seawater δ^{18}O and δD were initialized from constant values of -1‰ and -8‰, respectively (1). The 3X, 6X, and 9X simulations were integrated for 2,000 years and are described in refs. (23, 24). In addition, we extended each of these simulations for an additional 200 years using an updated formulation of the surface virtual salinity flux (see equation 7 from (25)), which better resolves the seawater salinity near river mouths and in the semi-enclosed Eocene Arctic Ocean. The 3X and 6X simulations were further branched into three experiments (respectively) with varying orbital parameters, including a minimum eccentricity and obliquity scenario (eccentricity = 0.0, obliquity = 22°), a high Northern Hemisphere seasonality scenario (eccentricity = 0.054, obliquity = 24.5°, perihelion during boreal summer), and a high Southern Hemisphere seasonality scenario (eccentricity = 0.054, obliquity = 24.5° perihelion during austral summer), following ref. (26). We also expanded the CO_2 sensitivity simulations by adding runs with 10X and 11X preindustrial CO_2, which were initialized from the 9X simulation and each integrated for 500 years. We note that the 10X simulation has not reached quasi-equilibrium and exhibits a trend in GMST of 0.3°C per century during the last 200 years. Also, the 11X simulation becomes unstable after year ~400 and a GMST of ~43°C with the top-of-atmosphere net radiation increasing with warming, indicating a "runaway greenhouse" effect in the model (Fig. S10). Although the 10X and 11X simulations are not in equilibrium, we decided to include them in the data assimilation to sample the superwarm,

75 low-possibility climate states. Table S2 gives a summary of these simulations and their boundary conditions; Figure S10
76 presents the time series of global mean surface temperature from all of these simulations.

77   50-year monthly and annual averages were drawn from each of these 14 simulations to use as the model prior in the data
78 assimilation for a total of 72 prior ensemble members. Specifically, we sampled the last 600 years of the 3X, 6X, and 9X
79 simulations (36 priors); the last 150 years of the extended versions of these experiments with a different virtual salinity flux (9
80 priors); the last 100 years of each orbital experiment at 3X and 6X (12 priors); the last 450 years of the 10X simulation (9
81 priors); and years 51-350 from the 11X simulation (6 priors, avoiding the end of the simulation that is unstable). The prior
82 sampling strategy was designed to ensure that all of the simulations were represented in the prior while also somewhat reducing
83 over-representation of the longest simulations (Fig. S10). Previous work has shown that offline DA results on long timescales
84 are not sensitive to the length of the time-average (27), thus we chose 50 years, consistent with our previous approach (27). We
85 note that even though GMST may be relatively similar between consecutive 50-yr periods from the same model experiment,
86 spatial patterns may differ in response to internal, multi-decadal variability. In addition to the model fields needed for proxy
87 forward modeling (sea-surface temperature (SST), sea-surface salinity (SSS), $\delta^{18}O_{sw}$; see below) we also included surface air
88 temperature (SAT; at 2m), precipitation, evaporation, the isotopes of precipitation ($\delta^{18}O$ and δD), snow thickness, and cloud
89 cover in the model prior so that those fields were updated by the data assimilation.

90 **Data assimilation.** The data assimilation method is an offline, ensemble square root Kalman filter approach, following the
91 methodology developed in refs. (27, 28) using the MATLAB code package DASH version 4.0.0, Alpha Test 5.0.6 (https:
92 //github.com/JonKing93/DASH). We refer the reader to these previous works for a full mathematical description. Briefly, the
93 posterior climate state (X_{post}, the reconstruction) is computed as a linear combination of the model prior states and the
94 information from the proxies, with a mean update equation of:

$$\bar{X}_{post} = \bar{X}_{prior} + K(y_{obs} - \bar{Y}_{est}) \tag{1}$$

96   X_{prior} is a $N \times M$ matrix containing the prior model states, where N contains all of the climate fields of interest (SST,
97 SAT, $\delta^{18}O_{sw}$, etc) collapsed into a "state vector", and M is the number of ensemble members (72 in this case). y_{obs} is a
98 $P \times 1$ vector containing the proxy data from each site at one point in time. Y_{est} is a $P \times M$ matrix of estimated proxy values,
99 forward-modeled from the model priors using Bayesian proxy models (2–5), for each site with a proxy and for each ensemble
100 member. To compute these values, we used the "analog mode" of the BAYSPAR calibration for TEX_{86} with a wide tolerance
101 of 12°C, and the annual, "all-species" models for both $\delta^{18}O$ and Mg/Ca, recognizing that the foraminifera are extinct species
102 and their seasonality of production is unknown.

103   Forward-modeling for TEX_{86} and $MBT^{5'}_{Me}$ is straightforward; only SST and SAT information from the model prior is
104 required, respectively. The $\delta^{18}O$ forward model requires SST and $\delta^{18}O_{sw}$, which are taken directly from the model prior, but
105 also requires constraints on surface ocean pH, which has been shown to influence foraminiferal $\delta^{18}O$ in culture studies (29) and
106 therefore is very likely to influence $\delta^{18}O$ excursions during the PETM (30). To accommodate the "pH effect," a function was
107 added to the BAYFOX forward modeling package to adjust $\delta^{18}O$ based on the theoretical equations provided by ref. (31). pH
108 values were drawn from the cGENIE simulation of ref. (32) for each core site, for the PETM and prePETM states, respectively.

109   The Mg/Ca proxy requires constraints on pH, bottom water saturation state (Ω), SSS, the Mg/Ca composition of seawater,
110 and the laboratory cleaning method. SSS was drawn from the model prior and the cleaning method is provided in the source
111 publications. The BAYMAG forward model has a built-in function to compute the Mg/Ca of seawater (4), which for the PETM
112 time (56 Ma) is 2.2. As with $\delta^{18}O$, pH values were drawn from cGENIE (32), along with bottom water Ω, using a documented
113 estimate of paleodepth for each core site.

114     $y_{obs} - \bar{Y}_{est}$ is the "innovation", the new information coming from the proxies, which is added to the prior state with a weight
115 of K, the Kalman gain:

$$K = cov(X_{prior}, Y_{est}) \times [cov(Y_{est}, Y_{est}) + R]^{-1} \tag{2}$$

117 where 'cov' denotes the covariance. The first term $cov(X_{prior}, Y_{est})$ describes the relationship between the prior state and
118 the forward-modeled proxy values, and effectively "spreads" the proxy information across the fields of interest. The second
119 term $[cov(Y_{est}, Y_{est}) + R]^{-1}$ contains the error terms, including the covariance of the estimated proxy values (Y_{est}) and the
120 proxy covariance (R). In this case, R is diagonal; i.e., the errors are assumed to be independent between proxies, following
121 (27, 28). R is user-defined, and ideally reflects an estimate of the "true" uncertainties of the proxies in the environment. The
122 Bayesian forward models provide a posterior value for proxy variance that represents the uncertainty associated with the
123 global core-top regressions that underlie these models; these values can be used for R. This error estimate is conservative, and
124 previous work applying data assimilation to Quaternary climate reconstruction found that posterior validation was improved
125 by scaling the Bayesian-derived uncertainty by about 1/5, with slightly different factors for different proxies (27, 28). However,
126 the climatic changes during the PETM are extreme; in the tropics, temperatures exceed the upper bounds of the modern
127 calibration datasets, and the organisms recording the proxy values were experiencing biological stress. Thus, we opt to use
128 values of R without any scaling. We make an exception to this for the $\delta^{18}O$ proxy, because initial leave-one-out validation
129 testing (see below) revealed no improvement in posterior RMSE for this proxy with $R = 0.35$ (a standard deviation of 0.59‰),
130 the error associated with the annual "all-species" BAYFOX model. We therefore scaled the error by a factor of 0.75 to $R = 0.26$,
131 the maximum value that produced improved internal validation in the posterior. The finding that $\delta^{18}O$ error may be smaller
132 than the BAYFOX estimate is qualitatively consistent with ref. (28), where validation exercises indicated that $\delta^{18}O$ was more
133 precise. The final R variances used for each proxy (in native proxy units) were 0.0045, 0.26, 0.046, and 0.0082 for TEX_{86}, $\delta^{18}O$,

Mg/Ca (in log units), and $MBT_{Me}^{5'}$, respectively. These translate into approximate 1σ SST uncertainties of 5.2°C for TEX_{86}, 2.2°C for $\delta^{18}O$, 3.3°C for Mg/Ca, and 3.5°C for $MBT_{Me}^{5'}$.

Validation. Given the limited proxy network, withholding 25% of the proxy data for internal validation, as was done in refs. (27, 28), was not practical. Instead, following ref. (33), we conducted leave-one-out experiments, in which each proxy was iteratively left out of the reconstruction and then the posterior result was used to forward-model the withheld proxy. Validation was assessed by comparing the root-mean-square-error (RMSE) of the posterior prediction against the prior prediction for the withheld proxies. For all four proxy types, RMSE improved in the posterior, indicating that the posterior solution represents a better match to the proxy information than the prior mean. RMSE improvement varied between proxy type with $MBT_{Me}^{5'}$, $\delta^{18}O$, Mg/Ca, and TEX_{86} improving by 3%, 3%, 19%, and 20%, respectively.

External validation is more useful and rigorous assessment of the reliability of the reconstruction. For this, we used estimates of PETM and prePETM temperatures in the deepMIP compilation (1) from terrestrial pollen, leaf-based, and clumped isotope proxies that were not assimilated (34–38). The posterior PETM-DA reproduces temperatures at these sites well ($R^2 = 0.95$) as shown in Fig. 2d. Notably, this validation score is higher than that of the prior mean ($R^2 = 0.70$, Fig. S5), indicating that the assimilation of the SST proxies resulted in a solution that is more consistent with the terrestrial proxy information. We also visually compared posterior $P - E$ to independent qualitative hydrological indicators of the sign of change (wetter or drier) from the compilation of ref. (39) with addition of data from ref. (7) (Fig. 3a). Finally, we compared posterior δD of precipitation to leaf wax δD_P proxies compiled in ref. (39) (Fig. 3c). These proxies provide an estimate of the change in the isotopes of precipitation, but at some sites the data do not indicate a clear excursion across the PETM. Thus, we plotted the average difference for sites where the PETM change exceeded $2\times$ the standard error range with colors that represent the size of the excursion, and for sites that did not meet this criteria, we plotted smaller white circles to indicate no significant change (Fig. 3c). The temperature, $P - E$, and leaf wax δD_P validation data may be found in Dataset S2.

Sensitivity Testing. Since the $\delta^{18}O$ and Mg/Ca proxy data require assumptions about the change in the ocean carbonate system during the PETM (see above) we investigated the sensitivity of the posterior PETM-DA GMST to these choices (Fig. S1). Our main result uses pH estimates from the cGENIE simulation of ref. (32), which simulates a drop in pH during the PETM of 0.3 units (from ca. 7.7 in the prePETM to 7.4 during the PETM). However the pH drop during the PETM could have been larger or smaller than indicated by this study. We therefore conducted DA experiments in which the pH change was increased to 0.5 units and decreased to 0.1 units, respectively, to assess whether the magnitude of this change affects our results. We found that GMST was not substantially affected by this choice (Fig. S1, ".5ΔpH" and ".1ΔpH"). Next, we tested the sensitivity of the DA to the choice of bottom water Ω (needed for forward modeling of Mg/Ca) by setting Ω to a value of 5 at each site, which effectively eliminates the impact of dissolution on the proxy (4). This resulted in slight lowering of absolute values of GMST (but still largely within error of the main results) and no change in ΔGMST (Fig. S1, "Omega5"). As discussed above, we discovered that inclusion of proxy data from *Acarinina spp.* lowers PETM GMST (but has little effect on prePETM GMST) thereby lowering ΔGMST to 4.4°C (Fig. S1, "Acarinina"). This is consistent with evidence that this species occupied a deeper part of the mixed layer during the PETM (16–18) and informed our decision to only use *Morozovella spp.* in our main PETM-DA result. To further test the sensitivity of the DA to the carbonate system assumptions, we conducted an experiment where values of ocean pH and Ω were held at modern values (drawn from the Global Ocean Data Analysis Project (GLODAP) version 2 (40), using the `omgph.m` function in `BAYMAG`). This choice lowers absolute GMST and ΔGMST, but not by much because the use of higher pH and lower Ω partly counteract each other (Fig. S1, "ModCarb"). We note that this is not realistic scenario, given that atmospheric CO_2 concentrations were certainly much higher than present during the late Paleocene/early Eocene.

Finally, we tested the sensitivity of the DA to assumptions surrounding the "pH effect" on foraminiferal $\delta^{18}O$ by conducting a DA experiment with the pH correction set to the low sensitivity exhibited by the extant planktic species *Orbulina universa* (29) ("LowpHSens" in Fig. S1) and by removing the pH effect entirely ("nopHCorr" in Fig. S1). In both cases absolute GMST is lower, especially for the PETM, since the drop in pH has less effect on $\delta^{18}O$ (Fig. S1). This results in a reduction of ΔGMST (Fig. S1). In our view, eliminating the pH correction entirely is not justified as culture studies of planktic and benthic foraminiferal species all show some sensitivity to changing pH (29, 41, 42). The reduced sensitivity of *Orbulina universa* (ca. 0.27‰ per pH unit) could conceivably be related to the fact that it is symbiont-bearing, with the photosynthetic symbionts acting to locally increase pH around the site of calcification (43). However, ref. (29) conducted experiments with *Orbulina* under both high light and dark conditions and there was no detectable difference in shell $\delta^{18}O$, seemingly ruling out a symbiont-related control. *Morozovella spp.* were also symbiont-bearing (44) which raises the possibility that they could have behaved like *Orbulina*, but given that, to the best of our knowledge, there are no additional published culture studies of other species of symbiont-bearing planktic foraminifera, and that ecology of *Morozovella spp.* is not precisely known, we prefer to use the thermodynamical pH effect correction (31) (ca. 1‰ per pH unit, between a pH of 7–8) in our main PETM-DA. This thermodynamical expectation also adequately explains the magnitude of the pH effect seen in cultures of the non-symbiont bearing *G. bulloides* (29) and symbiont-bearing benthic foraminifera (41, 42).

Climate Sensitivity Calculations. Following the framework of (45), we calculated climate sensitivity during the PETM relative to the prePETM, assuming CO_2 change is the sole forcing agent:

$$ECS_{PETM} = \Delta GMST \text{ / } CO_2 \text{ doublings} \quad\quad [3]$$

where

$$\text{CO}_2 \text{ doublings} = \log_2(PETM_{CO2}) - \log_2(prePETM_{CO2}) \qquad [4]$$

An ensemble estimate of ΔGMST is derived from the PETM-DA posterior. prePETM and PETM CO_2 concentrations were re-computed from the two available marine boron isotope (δ^{11}B) records that cover the event in temporal detail, from ODP 1209 (46) and DSDP 401 (32). Besides these boron isotope data, two other high-resolution records of CO_2 across the PETM exist. The reconstruction of (47) is based on B/Ca and δ^{11}B and thus is not independent from the δ^{11}B estimate we derive here; it also requires a double use of pH, hence the authors did not recommend its use for CO_2 reconstruction. The reconstruction of ref. (48) is based on carbon isotope measurements on terrestrial bulk organic matter, and thus is independent from marine proxies. However, this reconstruction method is relative—it requires an assumption to be made about starting concentrations of CO_2. ref. (48) assume that prePETM CO_2 was 338 ppm, which is not physically realistic considering the prePETM GMST we derive here (28.5°C). Moreover, use of higher plant-derived carbon isotopes to infer CO_2 is controversial, given evidence that plant carbon isotope fractionation also responds to aridity and that plants adapt to CO_2 on long geological timescales (49). Hence, we limit our analysis to the boron isotope data.

The δ^{11}B of planktic foraminifera is a proxy for the pH of surface seawater, which, in regions where dissolved CO_2 is in equilibrium with the atmosphere, is directly related to atmospheric CO_2 concentration. The computation of pH from δ^{11}B requires constraints on the δ^{11}B composition of seawater (δ^{11}B$_{sw}$), the equilibrium constant of boric acid (K_B), and the equilibrium fractionation between boric acid and borate. For the latter, we use the value of 27.2‰ from ref. (50). For δ^{11}B$_{sw}$, we use the estimate of 38.5‰ from ref. (51) with an uncertainty of 0.2‰ (1σ). K_B is a function of seawater state (temperature, salinity, pressure). Pressure is assumed to be 0 db; SST and SSS for each core site are drawn from the ensemble posterior of the PETM-DA. Computation of the carbonate system equilibrium constants also requires estimates of $[Ca^{2+}]$ and $[Mg^{2+}]$; for these we use the estimate of $[Mg^{2+}]$ from ref. (52) for 56 Ma and compute $[Ca^{2+}]$ assuming a Mg/Ca_{sw} ratio of 2.2, for consistency with the value used in the `BAYMAG` forward model for Mg/Ca.

The calculation of CO_2 from pH depends on SST and also requires an additional constraint on one other parameter of the ocean carbonate system. For SST, we use the posterior output from the PETM-DA at each core location, which is consistent with the estimate for GMST used for the climate sensitivity calculation. Moreover, computing SST from the raw proxy data at each site poses a circularity problem, since the Mg/Ca and δ^{18}O proxies require assumptions about surface ocean pH. The PETM-DA is constrained not only by Mg/Ca and δ^{18}O, but also by organic proxies that do not have a carbonate system dependency (TEX$_{86}$ and MBT$_{Me}^{5'}$), and is additionally subject to the constraints of the SST field covariance from the model prior. It is thus more independent from carbonate system assumptions (though not completely independent, since pH assumptions factor into forward modeling) and more robust than site-specific estimates.

Common choices for the second carbonate system parameter include alkalinity (*Alk*) (i.e., ref. (53)) and surface ocean saturation state (Ω) (i.e., ref. (51)). For the prePETM, we use Ω, and randomly sample from a wide uniform distribution of physically plausible values (between 5–8 (54)). These values are then used to compute CO_2 and *Alk* for the prePETM state. For the PETM, we leverage the carbonate chemistry solutions of the cGENIE simulations presented in ref. (32). These simulations were initialized with prePETM carbonate chemistry following refs. (55, 56), and then used both boron and carbon isotope constraints to fit the carbon emissions in the model to match the proxy-observed magnitude of the pH and carbon isotope excursion during the PETM. Although these results are partly fitted to the δ^{11}B-derived pH from Site 401 (which is used here to compute the change in CO_2) we use only the *relative* change in *Alk* simulated by ref. (32) which minimizes circularity. *Alk* is also a conservative property and thus not dependent on PETM ocean temperature. The simulated increase in *Alk* is 300 μmol kg^{-1}; this value is added to the prePETM *Alk* and then used to compute CO_2 during the PETM.

This approach allows both *Alk* and Ω to change during the PETM, consistent with proxy evidence for undersaturation (57, 58) and carbon modeling results (32, 56, 59). However, as a sensitivity test, we also consider two end-member scenarios in which either *Alk* or Ω is held constant between the prePETM and PETM. Both scenarios compute prePETM *Alk* and CO_2 using Ω, as described above. In the "Constant *Alk*" scenario, the prePETM *Alk* is then left unchanged and used to calculate PETM CO_2. This effectively assumes that carbonate and silicate weathering on land is too slow to contribute to a significant rise in *Alk* during the body of the PETM, which given the estimated time span of the PETM body (70–80 kyr; (60)) is not realistic. In the "Constant Ω" scenario, we simply use the same Ω values for the prePETM and PETM. This scenario is the opposite of "Constant *Alk*"; it assumes that weathering rapidly results in higher *Alk*, completely mitigating a drop in saturation state. As with the "Constant *Alk*" scenario, this is also not realistic given widespread evidence for ocean undersaturation and carbonate dissolution (57, 58). However, ref. (47) argue that this solution is plausible if the marine sites from which the δ^{11}B records derive are missing the peak of the event (and therefore the drop in Ω). Sedimentary loss has been reported at both of the sites with δ^{11}B data (DSDP 401 and ODP 1209), the former due to incomplete rotary drilling recovery (61) and the latter due to syndepositional dissolution and burndown (62), so this remains a possibility (albeit perhaps unlikely).

The "Constant *Alk*" scenario results in higher ECS (7.9°C; 6.9–9.3°C, 95% CI) (Fig. S6; Table S1) whereas "Constant Ω" results in the lower ECS (5.6°C; 4.8–6.7°C, 95% CI) (Fig. S9; Table S1). These results provide conservative upper and lower limits on what ECS could have been—i.e., it is unlikely to be either below 5 or above 9—and therefore support our conclusion in the main text that PETM ECS is higher than the IPCC AR6 90% CI range of 2–5°C.

Recognizing that the value of δ^{11}B$_{sw}$ is not yet securely known for the PETM time period, we also conducted sensitivity tests with δ^{11}B$_{sw}$ set to a lower value (38‰) and a higher value (39‰). These experiments show that the choice of δ^{11}B$_{sw}$ mainly impacts the absolute values of CO_2, with a lower δ^{11}B$_{sw}$ leading to lower CO_2 and vice versa. The δ^{11}B$_{sw}$ value has less of impact on CO_2 doublings and ECS, with the solutions for the latter only changing by 0.2–0.3°C (Table S1).

Since the calculation of climate sensitivity relies on the *change* in CO_2 relative to the prePETM base concentration (CO_2 doublings, Eq. 3), some of the uncertainties associated with the estimation of absolute values of CO_2 can be reduced by calculating the prePETM and PETM carbonate systems as a "pair". For example, given the long residence time of boron in seawater, $\delta^{11}B_{sw}$ can be assumed to not change through the event. Likewise, although the sampling of the carbonate system parameters is done separately for each site, the draws are carried through between the prePETM and PETM states, such that computation of ΔCO_2 eliminates the absolute uncertainty in these values. In this way, the uncertainty surrounding the calculation of CO_2 doublings is smaller than the uncertainties surrounding the absolute CO_2 concentrations estimated for each time period (Table S1, Fig. S9), as previously shown by ref. (63).

All calculations were conducted with 5,000 Monte Carlo simulations to fully sample the multiple sources of uncertainty ($\delta^{11}B_{sw}$, GMST, SST and SSS, and the second carbonate system parameter), following the methods in ref. (64). The code for these calculations is available on GitHub here: https://github.com/St-Andrews-Isotope-Geochemistry/PETM_deltaCO2.
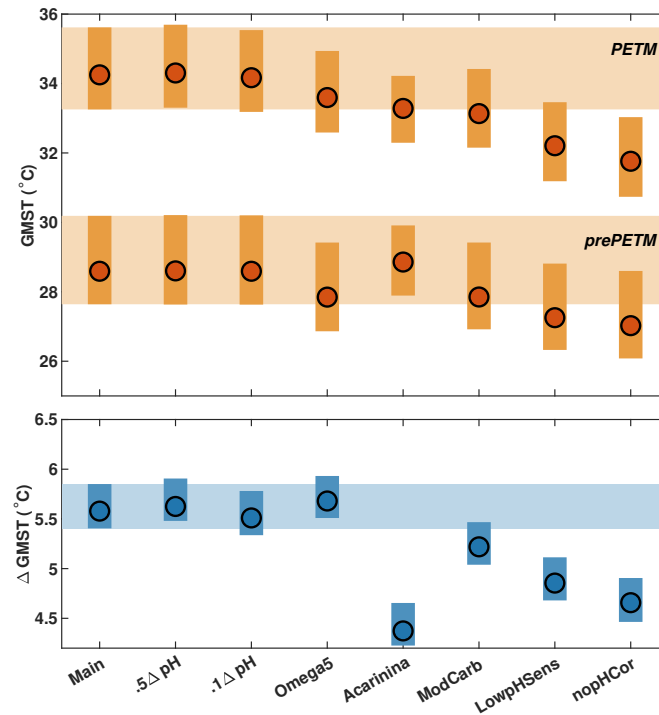
Fig. S1. Sensitivity testing for the PETM-DA in which different assumptions are made about the carbonate system for forward modeling of foraminiferal δ^{18}O and Mg/Ca. "Main" presents the results shown in the main text, which use carbonate system parameters drawn from cGENIE (32). ".5$\triangle$pH" increases the pH drop during the PETM to 0.5; ".1$\triangle$pH" decreases it to 0.1. "Omega5" sets the bottom water water saturation state (Ω) in the Mg/Ca forward model to 5 for all sites, effectively eliminating the influence of Ω on the proxy. "Acarinina" includes Mg/Ca and δ^{18}O data from *Acarinina spp.* (which are excluded from the Main result). "ModCarb" uses modern carbonate system parameters for Mg/Ca and δ^{18}O (drawn using the `omgph.m` function in BAYMAG). "LowpHSens" assumes that the δ^{18}O sensitivity to pH is smaller than predicted by thermodynamics, following experimental results with *Orbulina universa*. "nopHCor" assumes δ^{18}O is not sensitive to ocean pH. Top panel shows differences in absolute values of GMST for the PETM and prePETM respectively. Bottom panel shows differences in the change in GMST ($\triangle$GMST). For reference, light orange bands indicate Main values for PETM and prePETM GMST, light blue band indicates Main values for $\triangle$GMST. In all cases, error bounds represent the 95% confidence interval, dots show the median.
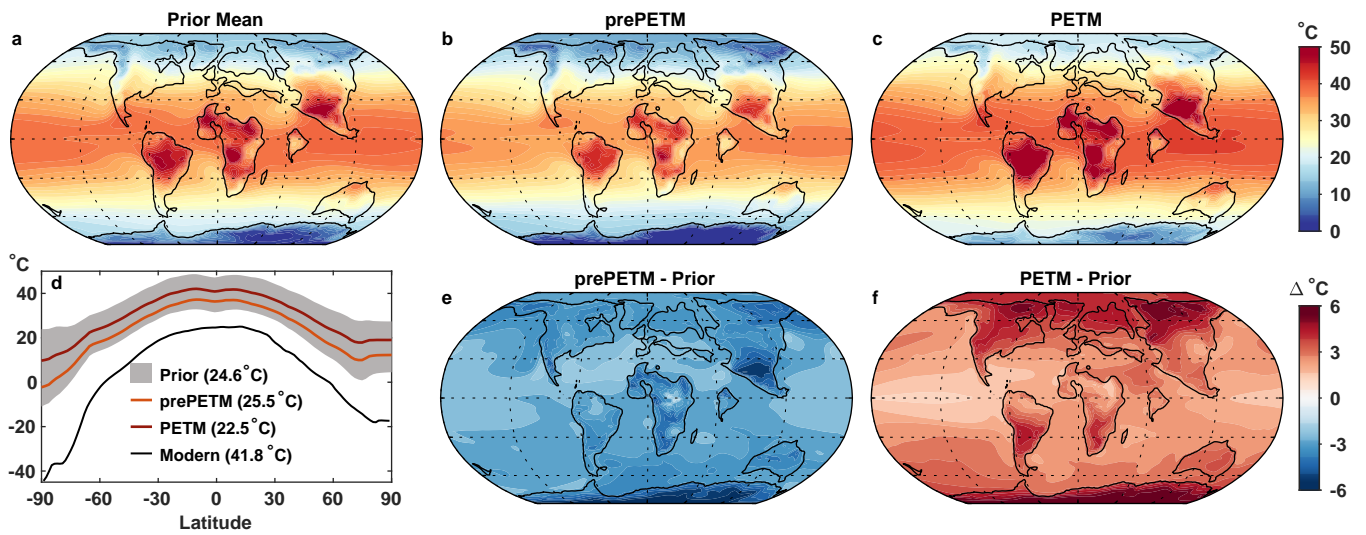
Fig. S2. Comparisons between the model prior and the prePETM and PETM DA posterior means for mean annual surface air temperature. a) Model prior mean annual SAT. b) Posterior mean annual SAT for the prePETM. c) Posterior mean annual SAT for the PETM. d) Zonal mean temperature for the full prior (in gray) vs. posterior means for the prePETM (orange) and PETM (red). Modern zonal mean SAT shown for reference (based on 2m air temperature from the ERA 20th Century Reanalysis (65)). Values in parentheses represent the meridional SAT gradient, calculated as average SAT between 30°S–30°N minus average SAT between 60–90°N and S. e) Difference plot between the prePETM - prior mean SAT. f) Difference plot between the PETM - prior mean SAT.
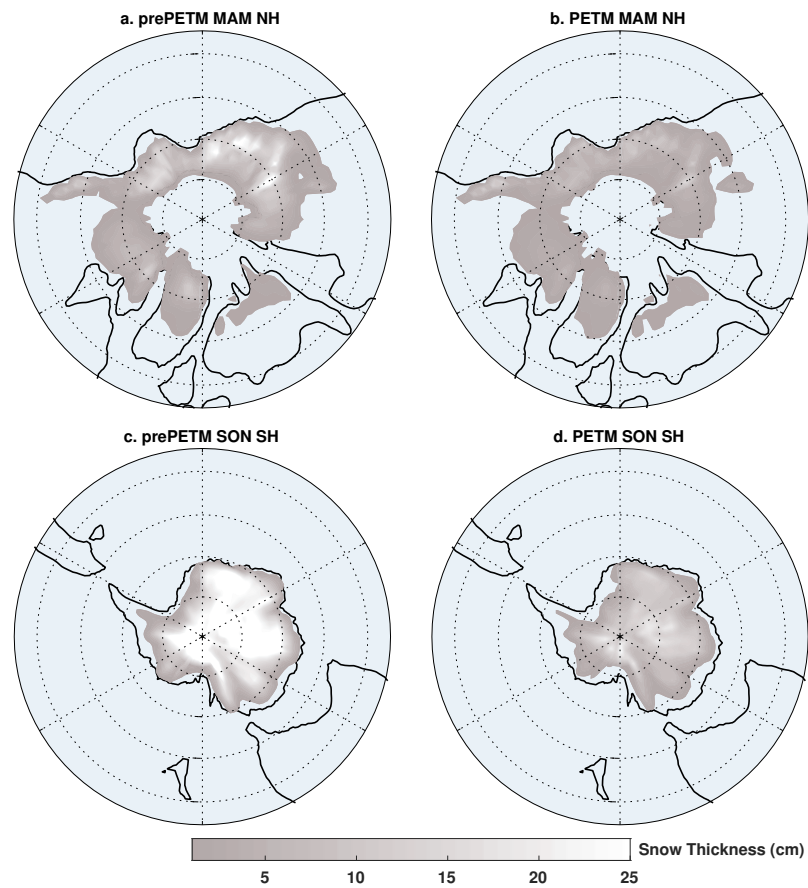
a. prePETM MAM NH

b. PETM MAM NH

c. prePETM SON SH

d. PETM SON SH

Snow Thickness (cm)

5   10   15   20   25

Fig. S3. Spring (MAM for the Northern Hemisphere, SON for the Southern Hemisphere) snow thickness from the PETM-DA, for the Northern Hemisphere (a and b) and the Southern Hemisphere (c and d) and prePETM (a and c) and PETM (b and d) time periods, respectively.
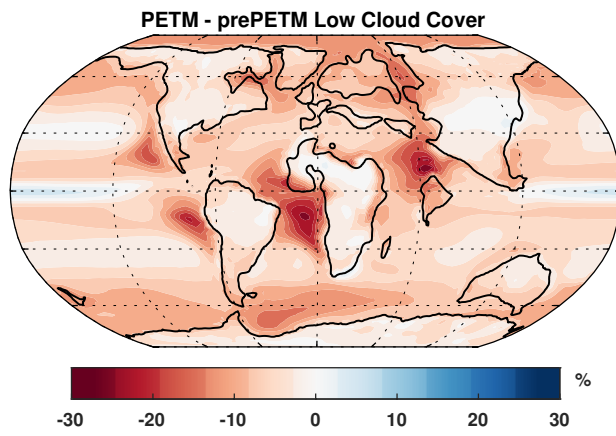
PETM - prePETM Low Cloud Cover

Fig. S4. Change in low cloud cover (%) in the PETM-DA, between the PETM and pre-PETM.
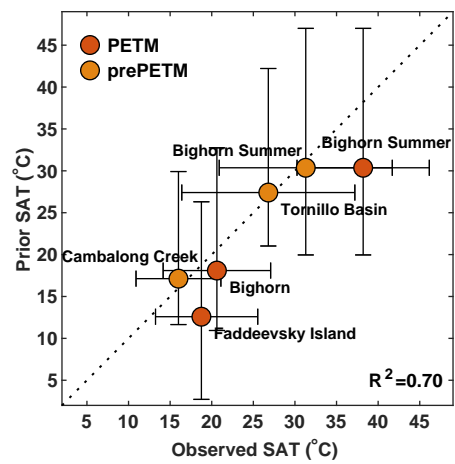
Fig. S5. Validation of the model prior against independent terrestrial temperature proxies (for comparison with Figure 2d).
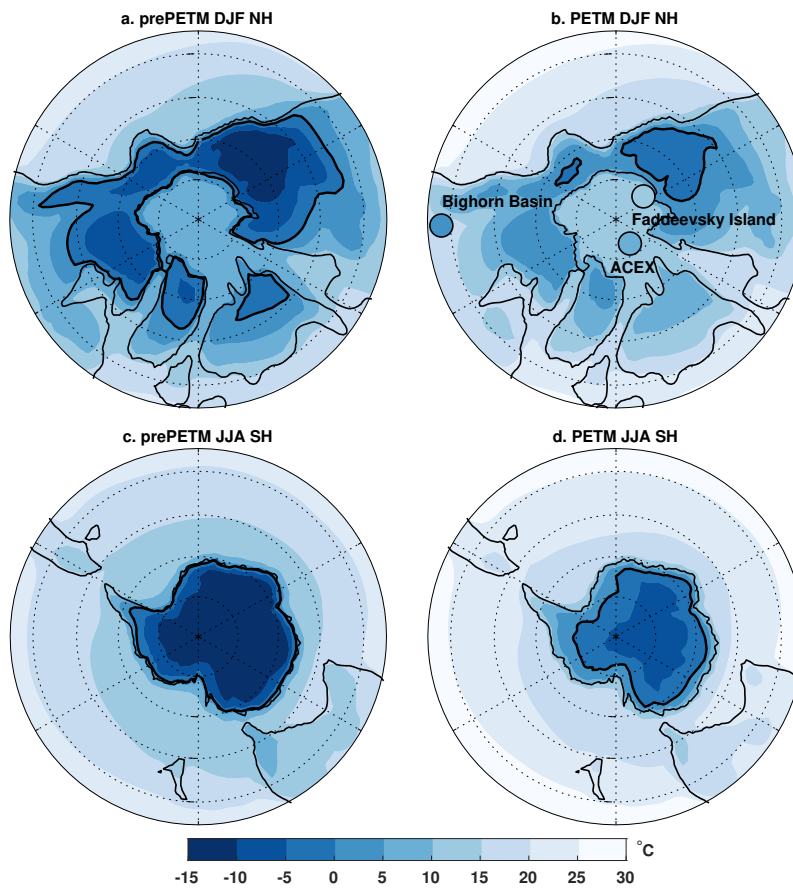
Fig. S6. Winter surface air temperatures (DJF for the Northern Hemisphere, JJA for the Southern Hemisphere) from the PETM-DA for the Northern Hemisphere (a and b) and the Southern Hemisphere (c and d) and prePETM (a and c) and PETM (b and d) time periods, respectively. Dots in panel b) show winter temperature estimates during the PETM from the Bighorn basin (35), Faddeevsky Island (34), and the ACEX core (66). Thick black lines indicate the 0°C contour.
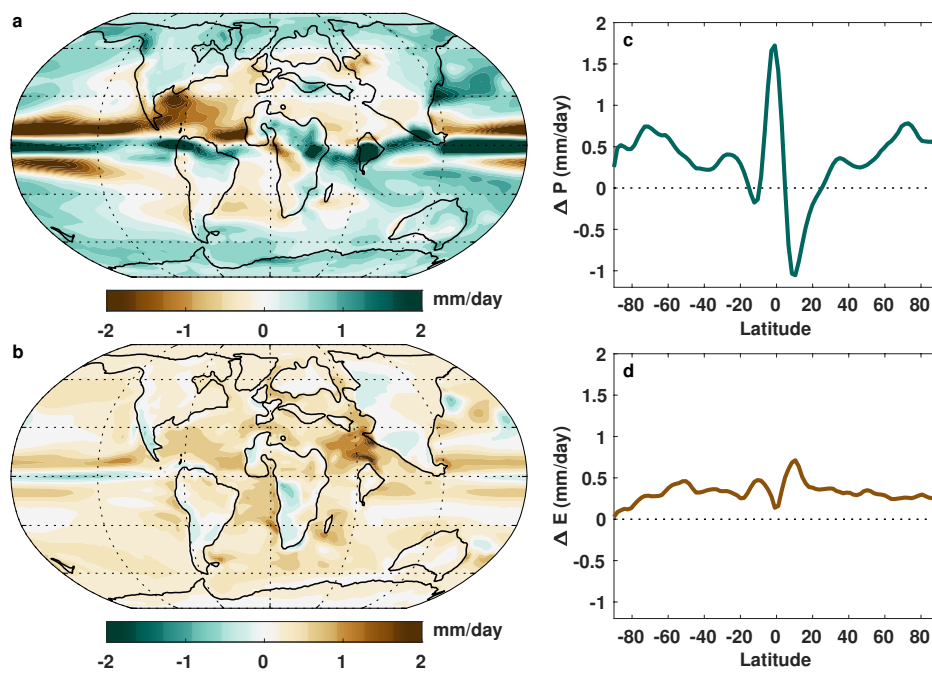
Fig. S7. Relative contribution of precipitation (P) and evaporation (E) to $P - E$ change during the PETM. a) mean annual change in P (PETM − prePETM) b) mean annual change in E (PETM − prePETM) c) zonal mean annual change in P d) zonal mean annual change in E.
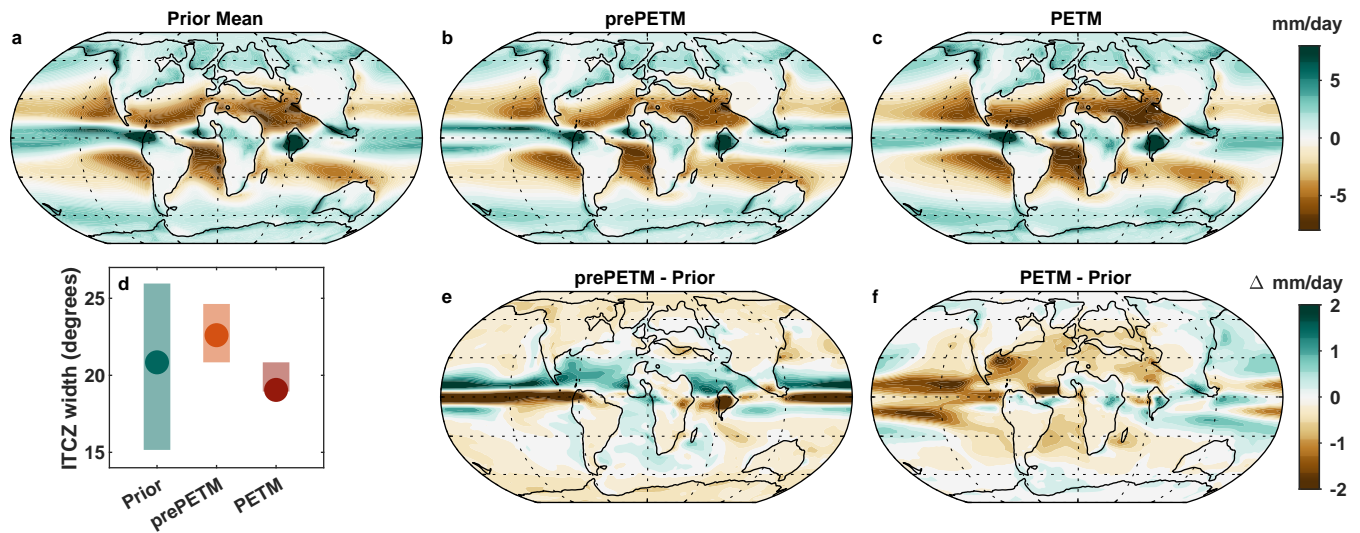
Fig. S8. Comparisons between the model prior and the prePETM and PETM DA posterior means for precipitation $-$ evaporation ($P - E$). a) Model prior mean annual $P - E$. b) Posterior mean annual $P - E$ for the prePETM. c) Posterior mean annual $P - E$ for the PETM. d) ITCZ width for the prior, prePETM, and PETM, calculated as the latitude degrees between 30 °S and 30 °N where $P - E > 0$. Dots represent the mean, error bars show the 95% confidence interval. e) Difference plot between the prePETM $-$ prior mean $P - E$. f) Difference plot between the PETM $-$ prior mean $P - E$.
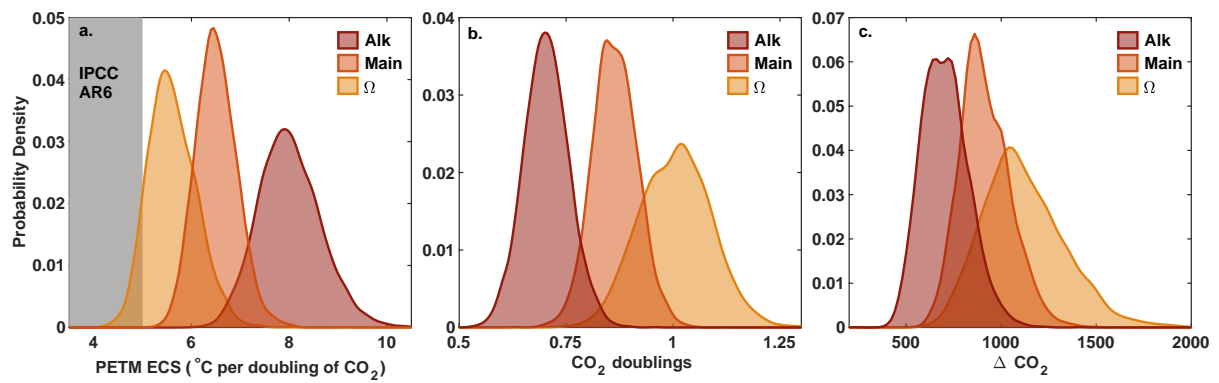
Fig. S9. Equilibrium climate sensitivity (ECS) for the PETM (a), calculated CO_2 doublings (b) and the change in CO_2 (c; ppm) between the PETM and prePETM, under three carbonate system scenarios. "Main" corresponds to the scenario shown in the main text. "Alk" and "Ω" correspond to the "Constant Alk" and "Constant Ω" end-member scenarios. The IPCC AR6 90% CI range for ECS is shown as a gray bar in panel a (67).
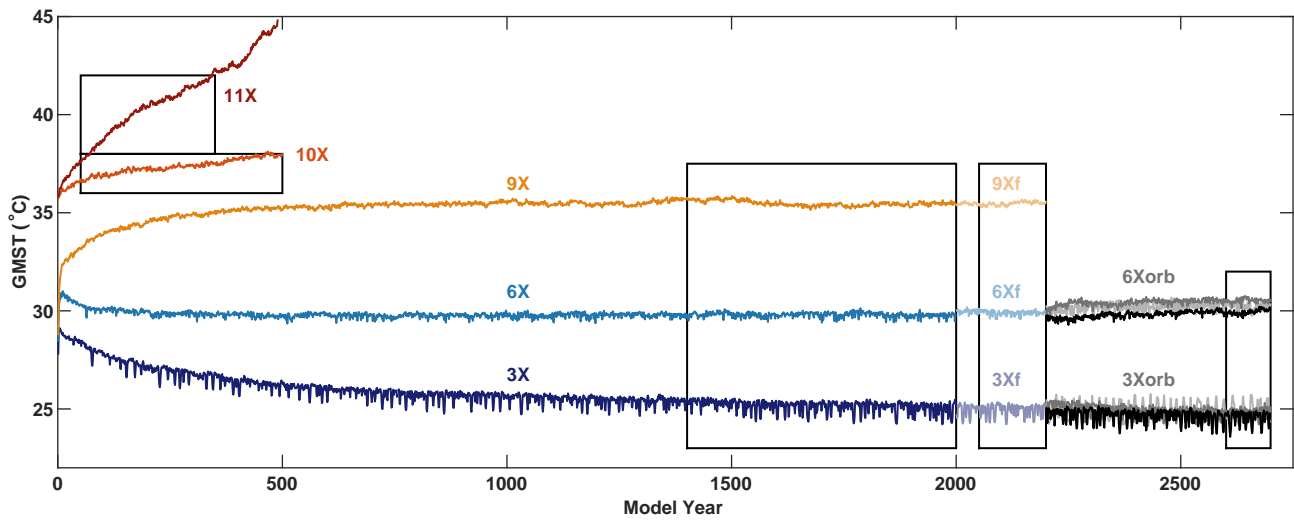
.

Fig. S10. Time series of global mean surface temperature (GMST) from all of the model experiments used as priors for the PETM-DA (Table S2). Boxes enclose the time periods that were sampled to generate the model priors. *N*X denotes *N* times preindustrial CO_2; *N*Xf denotes extended runs with a modified surface virtual salinity flux; *N*Xorb denotes runs with different orbital configurations. Note that, although they are plotted as starting at Year 0, the 10X and 11X experiments were branched from the long 9X experiment. The 11X experiment becomes unstable after ca. year 400 and a GMST of 43°C hence was not sampled during that interval. See the Supplementary text for details of these simulations.

Table S1. Median and 95% CI values (in parantheses) for prePETM and PETM CO_2 concentrations (ppm), the change in CO_2 ($\triangle CO_2$), the change in Alk ($\triangle Alk$; averaged between Sites 1209 and 401), the change in Ω ($\triangle\Omega$; averaged between Sites 1209 and 401), CO_2 Doublings, and equilibrium climate sensitivity (ECS) under different carbonate system scenarios. * indicates prescribed values.

Scenario	prePETM CO_2	PETM CO_2	$\triangle CO_2$	$\triangle$Alk	$\triangle\Omega$	CO_2 Doublings	ECS
Main	1120 (850–1460)	2020 (1550–2630)	900 (690–1200)	300*	−0.62 (−1.13−−0.19)	0.86 (0.76–0.97)	6.5 (5.7–7.4)
Constant Alk	1120 (850–1460)	1820 (1360–2410)	610 (380–940)	0*	−1.22 (−1.68−−0.82)	0.70 (0.60–0.81)	8.0 (6.9–9.3)
Constant Ω	1110 (850–1460)	2220 (1650–3010)	1090 (760–1590)	700 (500–970)	0*	1.01 (0.85–1.17)	5.6 (4.8–6.7)
δ^{11}Bsw = 38‰	840 (650–1090)	1500 (1180–1900)	660 (510–850)	300*	−0.33 (−0.79–0.07)	0.84 (0.74–0.94)	6.7 (5.9–7.7)
δ^{11}Bsw = 39‰	1520 (1150–2020)	2850 (2170–3790)	1330 (970–1820)	300*	−0.96 (−1.54−−0.46)	0.91 (0.80–1.03)	6.2 (5.4–7.1)

Table S2. Summary of the model simulations used to generate priors for the PETM-DA. Note that all simulations employed boundary conditions from deepMIP ([21]), including Eocene paleogeography, land-sea mask, and vegetation distribution ([22]), and preindustrial non-CO_2 greenhouse gas concentrations, solar constant, soil properties, and natural aerosol emissions. Orbital parameters used in the simulations are listed, including the eccentricity (e), obliquity (o), and precession (in longitude of the perihelion, ω; for example, $\omega = 270°$ means that perihelion occurs at the Northern Hemisphere solstice). See the "Supplementary text" for details of these simulations.

Experiment	CO_2 (ppm)	Orbital Parameters	Virtual Salinity Flux	Length (yr)	# of priors	Citation
3X	854	preindustrial	standard	2000	12	([23, 24])
3Xf	854	preindustrial	adjusted	200	3	This study
3Xorbmin	854	$e = 0; o = 22°$	adjusted	500	2	This study
3XorbmaxN	854	$e = 0.054; o = 24.5°; \omega = 270°$	adjusted	500	2	This study
3XorbmaxS	854	$e = 0.054; o = 24.5°; \omega = 90°$	adjusted	500	2	This study
6X	1708	preindustrial	standard	2000	12	([23, 24])
6Xf	1708	preindustrial	adjusted	200	3	This study
6Xorbmin	1708	$e = 0; o = 22°$	adjusted	500	2	This study
6XorbmaxN	1708	$e = 0.054; o = 24.5°; \omega = 270°$	adjusted	500	2	This study
6XorbmaxS	1708	$e = 0.054; o = 24.5°; \omega = 90°$	adjusted	500	2	This study
9X	2562	preindustrial	standard	2000	12	([23, 24])
9Xf	2562	preindustrial	adjusted	200	3	This study
10X	2847	preindustrial	adjusted	500	9	This study
11X	3132	preindustrial	adjusted	500	6	This study

SI Dataset S1 (DatasetS1.csv)

Paleoclimate proxy data used in the PETM-DA, including metadata (site name, modern location, paleo-location, source references).

SI Dataset S2 (DatasetS2.xlsx)

Independent proxy data used to validate the PETM-DA, including the terrestrial temperature data shown in Figure 2d, the hydrological proxy data shown in Figure 3a, and the leaf wax δD_P data shown in Figure 3c.

References

1. CJ Hollis, et al., The DeepMIP contribution to PMIP4: methodologies for selection, compilation and analysis of latest Paleocene and early Eocene climate proxy data, incorporating version 0.1 of the DeepMIP database. *Geosci. Model. Dev.* **12**, 3149–3206 (2019).

2. JE Tierney, MP Tingley, A Bayesian, spatially-varying calibration model for the TEX$_{86}$ proxy. *Geochimica et Cosmochimica Acta* **127**, 83–106 (2014).

3. SB Malevich, L Vetter, JE Tierney, Global Core Top Calibration of δ^{18}O in Planktic Foraminifera to Sea Surface Temperature. *Paleoceanogr. Paleoclimatology* **34**, 1292–1315 (2019).

4. JE Tierney, SB Malevich, W Gray, L Vetter, K Thirumalai, Bayesian calibration of the Mg/Ca paleothermometer in planktic foraminifera. *Paleoceanogr. Paleoclimatology* **34**, 2005–2030 (2019).

5. ED Crampton-Flood, JE Tierney, F Peterse, FM Kirkels, JS Sinninghe Damsté, BayMBT: A Bayesian calibration model for branched glycerol dialkyl glycerol tetraethers in soils and peats. *Geochimica et Cosmochimica Acta* **268**, 142–159 (2020).

6. EW Stokke, MT Jones, JE Tierney, HH Svensen, JH Whiteside, Temperature changes across the Paleocene-Eocene Thermal Maximum–a new high-resolution TEX$_{86}$ temperature record from the Eastern North Sea Basin. *Earth Planet. Sci. Lett.* **544**, 116388 (2020).

7. V Smith, et al., Life and death in the Chicxulub impact crater: a record of the Paleocene–Eocene Thermal Maximum. *Clim. Past* **16**, 1889–1899 (2020).

8. A Sluijs, et al., Late Paleocene–early Eocene Arctic Ocean sea surface temperatures: reassessing biomarker paleothermometry at Lomonosov Ridge. *Clim. Past* **16**, 2381–2400 (2020).

9. JS Barnet, et al., Coupled evolution of temperature and carbonate chemistry during the Paleocene–Eocene; new trace element records from the low latitude Indian Ocean. *Earth Planet. Sci. Lett.* **545**, 116414 (2020).

10. R Kozdon, et al., Enhanced poleward flux of atmospheric moisture to the Weddell Sea region (ODP site 690) during the Paleocene-Eocene thermal maximum. *Paleoceanogr. Paleoclimatology* **35**, e2019PA003811 (2020).

11. E Huurdeman, et al., Rapid expansion of meso-megathermal rain forests into the southern high latitudes at the onset of the Paleocene-Eocene Thermal Maximum. *Geology* **49**, 40–44 (2021).

12. GN Inglis, et al., Terrestrial methane cycle perturbations during the onset of the Paleocene-Eocene Thermal Maximum. *Geology* **49**, 520–524 (2021).

13. EC Hopmans, et al., A novel proxy for terrestrial organic matter in sediments based on branched and isoprenoid tetraether lipids. *Earth Planet. Sci. Lett.* **224**, 107–116 (2004).

14. YG Zhang, et al., Methane index: A tetraether archaeal lipid biomarker indicator for detecting the instability of marine gas hydrates. *Earth Planet. Sci. Lett.* **307**, 525–534 (2011).

15. PL Schoon, C Heilmann-Clausen, BP Schultz, JSS Damste, S Schouten, Warming and environmental changes in the eastern North Sea Basin during the Palaeocene–Eocene Thermal Maximum as revealed by biomarker lipids. *Org. Geochem.* **78**, 79–88 (2015).

16. A Bornemann, et al., Persistent environmental change after the Paleocene–Eocene Thermal Maximum in the eastern North Atlantic. *Earth Planet. Sci. Lett.* **394**, 70–81 (2014).

17. M Makarova, et al., Hydrographic and ecologic implications of foraminiferal stable isotopic response across the US mid-Atlantic continental shelf during the Paleocene-Eocene Thermal Maximum. *Paleoceanography* **32**, 56–73 (2017).

18. W Si, MP Aubry, Vital effects and ecologic adaptation of photosymbiont-bearing planktonic foraminifera during the Paleocene-Eocene thermal maximum, implications for paleoclimate. *Paleoceanogr. Paleoclimatology* **33**, 112–125 (2018).

19. JW Hurrell, et al., The community Earth system model: a framework for collaborative research. *Bull. Am. Meteorol. Soc.* **94**, 1339–1360 (2013).

20. E Brady, et al., The connected isotopic water cycle in the Community Earth System Model version 1. *J. Adv. Model. Earth Syst.* **11**, 2547–2566 (2019).

21. DJ Lunt, et al., The DeepMIP contribution to PMIP4: experimental design for model simulations of the EECO, PETM, and pre-PETM (version 1.0). *Geosci. Model. Dev.* **10**, 889–901 (2017).

22. N Herold, et al., A suite of early Eocene ($\sim$ 55 Ma) climate model boundary conditions. *Geosci. Model. Dev.* **7**, 2077–2090 (2014).

23. J Zhu, CJ Poulsen, JE Tierney, Simulation of Eocene extreme warmth and high climate sensitivity through cloud feedbacks. *Sci. Adv.* **5**, eaax1874 (2019).

24. J Zhu, et al., Simulation of early Eocene water isotopes using an Earth system model and its implication for past climate reconstruction. *Earth Planet. Sci. Lett.* **537**, 116164 (2020).
25. Yh Tseng, FO Bryan, MM Whitney, Impacts of the representation of riverine freshwater input in the community Earth system model. *Ocean. Model.* **105**, 71–86 (2016).
26. DJ Lunt, et al., A model for orbital pacing of methane hydrate destabilization during the Palaeogene. *Nat. Geosci.* **4**, 775–778 (2011).
27. JE Tierney, et al., Glacial cooling and climate sensitivity revisited. *Nature* **584**, 569–573 (2020).
28. MB Osman, et al., Globally resolved surface temperatures since the Last Glacial Maximum. *Nature* **599**, 239–244 (2021).
29. HJ Spero, J Bijma, DW Lea, BE Bemis, Effect of seawater carbonate concentration on foraminiferal carbon and oxygen isotopes. *Nature* **390**, 497–500 (1997).
30. J Uchikawa, RE Zeebe, Examining possible effects of seawater pH decline on foraminiferal stable isotopes during the Paleocene-Eocene Thermal Maximum. *Paleoceanography* **25** (2010).
31. R Zeebe, An expression for the overall oxygen isotope fractionation between the sum of dissolved inorganic carbon and water. *Geochem. Geophys. Geosystems* **8** (2007).
32. M Gutjahr, et al., Very large release of mostly volcanic carbon during the Palaeocene–Eocene Thermal Maximum. *Nature* **548**, 573–577 (2017).
33. JM King, et al., A data assimilation approach to last millennium temperature field reconstruction using a limited high-sensitivity proxy network. *J. Clim.* **34**, 7091—-7111 (2021).
34. G Suan, et al., Subtropical climate conditions and mangrove growth in Arctic Siberia during the early Eocene. *Geology* **45**, 539–542 (2017).
35. KE Snell, et al., Hot summers in the Bighorn Basin during the early Paleogene. *Geology* **41**, 55–58 (2013).
36. DJ Peppe, et al., Sensitivity of leaf size and shape to climate: global patterns and paleoclimatic applications. *New phytologist* **190**, 724–739 (2011).
37. JR Kelson, et al., Warm terrestrial subtropics during the Paleocene and Eocene: Carbonate clumped isotope ($\Delta 47$) evidence from the Tornillo Basin, Texas (USA). *Paleoceanogr. Paleoclimatology* **33**, 1230–1249 (2018).
38. DR Greenwood, PT Moss, AI Rowett, AJ Vadala, RL Keefe, Plant communities and climate change in southeastern Australia during the early Paleogene. *Special Pap. Geol. Soc. Am.* **369**, 365–380 (2003).
39. MJ Carmichael, et al., Hydrological and associated biogeochemical consequences of rapid global warming during the Paleocene-Eocene Thermal Maximum. *Glob. Planet. Chang.* **157**, 114–138 (2017).
40. SK Lauvset, et al., A new global interior ocean mapped climatology: The 1×1 GLODAP version 2. *Earth Syst. Sci. Data* **8**, 325–340 (2016).
41. C Rollion-Bard, J Erez, T Zilberman, Intra-shell oxygen isotope ratios in the benthic foraminifera genus Amphistegina and the influence of seawater carbonate chemistry and temperature on this ratio. *Geochimica et Cosmochimica Acta* **72**, 6006–6014 (2008).
42. LL Robbins, P Knorr, J Wynn, P Hallock, P Harries, Interpreting the role of pH on stable isotopes in large benthic foraminifera. *ICES J. Mar. Sci.* **74**, 955–964 (2017).
43. J Bijma, H Spero, D Lea, Reassessing foraminiferal stable isotope geochemistry: Impact of the oceanic carbonate system (experimental results) in *Use of proxies in paleoceanography: Examples from the South Atlantic*, eds. G Fischer, G Weber. (Springer), pp. 489–512 (1999).
44. T Aze, et al., A phylogeny of Cenozoic macroperforate planktonic foraminifera from fossil data. *Biol. Rev.* **86**, 900–927 (2011).
45. G Shaffer, M Huber, R Rondanelli, JO Pepke Pedersen, Deep time evidence for climate sensitivity increase with warming. *Geophys. Res. Lett.* **43**, 6538–6545 (2016).
46. DE Penman, B Hönisch, RE Zeebe, E Thomas, JC Zachos, Rapid and sustained surface ocean acidification during the Paleocene-Eocene Thermal Maximum. *Paleoceanography* **29**, 357–369 (2014).
47. LL Haynes, B Hönisch, The seawater carbon inventory at the Paleocene–Eocene Thermal Maximum. *Proc. Natl. Acad. Sci.* **117**, 24088–24095 (2020).
48. Y Cui, BA Schubert, Towards determination of the source and magnitude of atmospheric pCO2 change across the early Paleogene hyperthermals. *Glob. Planet. Chang.* **170**, 120–125 (2018).
49. K Schlanser, et al., On geologic timescales, plant carbon isotope fractionation responds to precipitation similarly to modern plants and has a small negative correlation with pCO_2. *Geochimica et Cosmochimica Acta* **270**, 264–281 (2020).
50. K Klochko, AJ Kaufman, W Yao, RH Byrne, JA Tossell, Experimental measurement of boron isotope fractionation in seawater. *Earth Planet. Sci. Lett.* **248**, 276–285 (2006).
51. E Anagnostou, et al., Changing atmospheric CO_2 concentration was the primary driver of early Cenozoic climate. *Nature* **533**, 380–384 (2016).
52. RE Zeebe, T Tyrrell, History of carbonate ion concentration over the last 100 million years II: Revised calculations and new data. *Geochimica et Cosmochimica Acta* **257**, 373–392 (2019).
53. MA Martínez-Botí, et al., Plio-Pleistocene climate sensitivity evaluated using high-resolution CO_2 records. *Nature* **518**, 49–54 (2015).
54. A Ridgwell, A Mid Mesozoic Revolution in the regulation of ocean chemistry. *Mar. Geol.* **217**, 339–357 (2005).
55. K Panchuk, A Ridgwell, L Kump, Sedimentary response to Paleocene-Eocene Thermal Maximum carbon release: A

382 model-data comparison. *Geology* **36**, 315–318 (2008).

56. A Ridgwell, DN Schmidt, Past constraints on the vulnerability of marine calcifiers to massive carbon dioxide release. *Nat. Geosci.* **3**, 196–200 (2010).

57. JC Zachos, et al., Rapid acidification of the ocean during the Paleocene-Eocene thermal maximum. *Science* **308**, 1611–1615 (2005).

58. TJ Bralower, et al., Evidence for shelf acidification during the onset of the Paleocene-Eocene thermal maximum. *Paleoceanogr. Paleoclimatology* **33**, 1408–1426 (2018).

59. Y Cui, et al., Slow release of fossil carbon during the Palaeocene–Eocene Thermal Maximum. *Nat. Geosci.* **4**, 481–485 (2011).

60. U Röhl, T Westerhold, TJ Bralower, JC Zachos, On the duration of the Paleocene-Eocene thermal maximum (PETM). *Geochem. Geophys. Geosystems* **8** (2007).

61. TL Babila, et al., Capturing the global signature of surface ocean acidification during the Palaeocene–Eocene Thermal Maximum. *Philos. Transactions Royal Soc. A: Math. Phys. Eng. Sci.* **376**, 20170072 (2018).

62. TJ Bralower, et al., Impact of dissolution on the sedimentary record of the Paleocene–Eocene thermal maximum. *Earth Planet. Sci. Lett.* **401**, 70–82 (2014).

63. GL Foster, JW Rae, Reconstructing ocean pH with boron isotopes in foraminifera. *Annu. Rev. Earth Planet. Sci.* **44**, 207–237 (2016).

64. JW Rae, et al., Atmospheric CO_2 over the past 66 million years from marine archives. *Annu. Rev. Earth Planet. Sci.* **49**, 609–641 (2021).

65. P Poli, et al., ERA-20C: An atmospheric reanalysis of the twentieth century. *J. Clim.* **29**, 4083–4097 (2016).

66. DA Willard, et al., Arctic vegetation, temperature, and hydrology during Early Eocene transient global warming events. *Glob. Planet. Chang.* **178**, 139–152 (2019).

67. P Forster, et al., The Earth's energy budget, climate feedbacks, and climate sensitivity in *Climate Change 2021: The Physical Science Basis. Working Group I contribution to the Sixth Assessment Report of the Intergovernmental Panel on Climate Change*, eds. V Masson-Delmotte, et al. (Cambridge University Press, Cambridge, United Kingdom), (2021).